DOI 10.5162/sensoren2024/D3.3

Magnetically Enhanced Ultrasound Strain Elastography to Visualize Magnetic Nanoparticles

Christian Marinus Huber[1,2], Melina Sophie Müller[2], Helmut Ermert[1], Christian Heim[3], Stefan J. Rupitsch[3] , Ingrid Ullmann[2] and Stefan Lyer[1]
[1]Department of Otorhinolaryngology, Head and Neck Surgery, Section of Experimental Oncology and Nanomedicine (SEON), Professorship for AI-Controlled Nanomaterials (KINAM), Universitätsklinikum Erlangen, Germany
[2]Institute of Microwaves and Photonics (LHFT), Friedrich-Alexander-Universität Erlangen-Nürnberg
[3]Department of Microsystems Engineering (IMTEK), Laboratory for Electrical Instrumentation and Embedded Systems, University of Freiburg
{Christian.Huber; Stefan.Lyer}@uk-erlangen.de, {Melina.Müller; Helmut.Ermert; Ingrid.Ullmann}@fau.de, {Christian.Heim; Stefan.Rupitsch}@imtek.uni-freiburg.de

Abstract

This study explores the potential of Magnetically enhanced Ultrasound Strain Elastography (MUSE) for visualizing the distribution of magnetic nanoparticles (MNPs) employed in magnetic drug targeting (MDT). MDT leverages MNPs as drug carriers, accumulated by an external magnetic field at the target site, typically a tumor. The localized accumulation of these particles alters the effective elastic properties of the tissue, potentially enabling visualization through ultrasound strain imaging, which maps local variations in elasticity. However, a direct link between MNPs and regions of increased stiffness has yet to be established. This work proposes MUSE as a solution, utilizing an external magnetic field to manipulate MNP distribution and consequently, tissue elasticity. The feasibility of MUSE was assessed using a polyvinyl alcohol ultrasound phantom containing an MNP inclusion. The results demonstrated successful mapping of the inclusion using the proposed method.

Keywords: Medical Technology, Ultrasound Imaging, Cancer Therapy, Magnetic Nanoparticles, Magnetic Durg Targeting

1. Introduction

Cancer is one of the leading causes of mortality worldwide, ranking second only to heart diseases [1]. The standard treatment options typically include radiation therapy, hyperthermia, surgical removal, or chemotherapy. In chemotherapy, therapeutic agents are administered systemically, affecting the entire body, which can result in damage to healthy cells and overall health deterioration.
A promising approach to mitigate these side effects is localized chemotherapy using magnetic nanoparticles (MNPs), known as Magnetic Drug Targeting (MDT) [2]. In MDT, chemotherapeutic agents are bound to nanoscale magnetic particles and accumulated at the tumor site using an external magnetic field. This method has shown considerable advantages over traditional systemic approaches [3]. Nevertheless, further advancements are crucial to unlock its full potential. Key areas for improvement in MDT include:

- **Accumulation process**: Optimizing the process by which MNPs are guided to the target site remains crucial. While current methods utilize external magnetic fields, ultrasound technology [4] and improved magnet designs [5] hold promise for further refinements.

- **Local drug release:** Efficient and localized release of the therapeutic payload specifically at the tumor site is critical for maximizing therapeutic benefit. Ultrasound-mediated cavitation offers a promising strategy for achieving this [6, 7].

- **Therapy monitoring**: Accurately detecting and mapping the spatial distribution of MNPs is essential for optimizing drug dosage, ensuring complete tumor eradication, and preventing potential side effects. This study focuses on developing a novel method for effective therapy monitoring.

Traditional imaging techniques, such as magnetic resonance imaging [8] and magnetic particle imaging [9], are not ideal for monitoring MDT due to interference from the external magnetic field and logistical challenges in

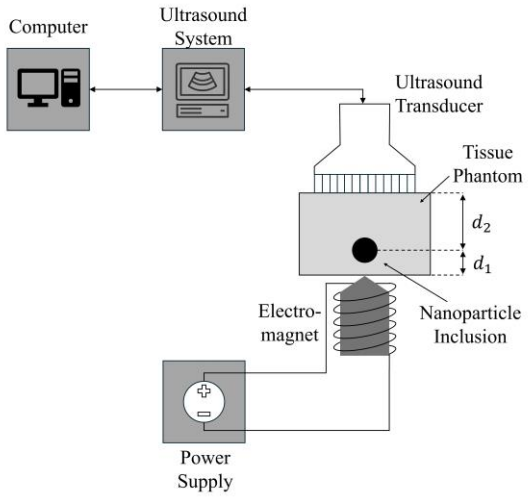

Fig. 1: Measurement setup used for magnetically enhanced ultrasound elastography.

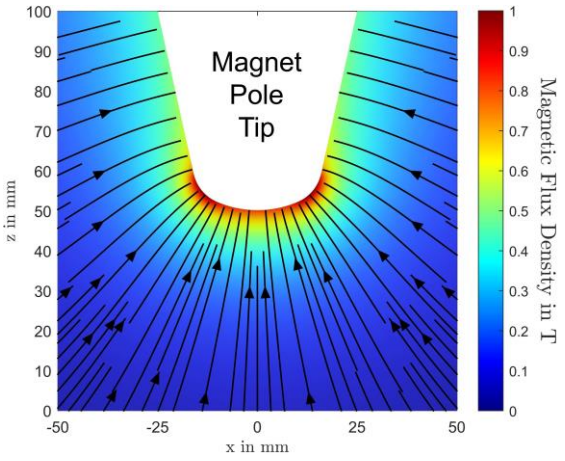

Fig. 2: Simulated magnetic flux density field of the MDT-electromagnet used in this contribution. The arrow lines mark the direction of the magnetic flux density gradient.

accommodating the therapy setup within these imaging devices.

In contrast, ultrasound-based methods offer effective and cost-efficient alternatives, such as magnetomotive ultrasound (MMUS) [10, 11], photoacoustic imaging [12] or ultrasound strain elastography (USE) [13].

USE holds advantages compared to other ultrasound-based methods, as it is a real-time modality and is already widely integrated into modern clinical ultrasound systems. This technique maps the mechanical properties of biological tissues [14]. Our previous study demonstrated a potential link between regions of increased stiffness and MNP presence [13].

A crucial challenge remains in verifying whether these stiffer regions definitively correspond to MNP distributions. To address this, we propose a novel approach – magnetically enhanced ultrasound strain elastography (MUSE).

MUSE leverages the inherent magnetic properties of MNPs by utilizing the static magnetic field already present during MDT therapy. This technique establishes a clear correlation between observed stiff areas and the actual distribution of MNPs. Notably, MUSE remains effective even in scenarios where conventional USE fails to detect any stiffness variations, offering a robust and reliable method for therapy monitoring in MDT.

2. Methods and Materials

The setup illustrated in Fig. 1 was utilized to assess the effectiveness of MUSE in visualizing MNPs. A computer gathered data from the ultrasound system (Verasonics Vantage 64 LE), linked to a linear array transducer (L11-5v, Verasonics). This transducer features a center frequency of 7.6 MHz, a relative bandwidth of 77 %, and an element pitch of 0.3 mm. Positioned above the ultrasound phantom, the transducer was mounted on a mechanical linear unit for precise control of the compression level during ultrasound strain imaging. Beneath the ultrasound phantom, an MDT-electromagnet was positioned [3, 15]. The electromagnet was powered by a DC power supply, which could be switched between a DC current of 70 A (representing the "Magnet on" state) and no current (representing the "Magnet off" state) for the measurements. Fig. 2 displays a simulation (COMSOL Multiphysics) illustrating the magnetic flux density field of the MDT-electromagnet at 70 A coil current. Within this simulation, the maximum field strength reaches approximately 1 T, directly at the tip of the magnetic pole. The magnetic force is proportional to the magnetic gradient field, which is depicted through a series of arrow lines in Fig. 2, providing a visual representation of the magnetic force.

2.1 Tissue mimicking ultrasound phantom

The tissue-mimicking ultrasound phantom was created using polyvinyl alcohol (PVA) powder (Kuraray, elvanol 71-30), dextran magnetic nanoparticle suspension, graphite scatterer (ProGraphiteShop, spherical Graphite, size ~10 µm), and ultra-pure water. The phantom adopted a cubic shape (outer phantom) with dimensions of $(x, y, z) =$ (50 mm, 25 mm, 50 mm). A cylindrical inclusion (inner phantom), either containing MNPs or devoid of them, spanned the entire depth (25 mm) with a diameter of 10 mm. As depicted in Fig. 1, the phantom was positioned below the ultrasound

transducer, with $d_2 = 35$ mm and $d_1 = 15$ mm. Two different phantoms were created for the measurements, with one containing MNPs and the other serving as a control phantom without MNPs. This ensured that any discrepancies in stiffness were not due to the construction process. The measurement process (which is described in Section 2.3 *Ultrasound Strain Elastography* and illustrated in Tab. 1) was repeated three times, each with newly constructed phantoms, which resulted in a total of six phantoms.
The construction method, adapted from [16], began with the outer ultrasound phantom. A mixture of 10 wt% PVA powder, 1 wt% graphite, and 94 wt% ultra-pure water was heated to 80 °C with continuous stirring. This mixture was then poured into a cubic mold with a cylindrical recess and placed in a vacuum chamber to remove any potential air inclusions. Two such outer ultrasound phantoms were created at the same time using this process.
After this, the inner inclusion was constructed, following similar steps. One inclusion was prepared using the same ingredients as the outer phantom, while a second one incorporated 5 (mg Fe)/mL of MNPs. This mixture consisted of 10 wt% PVA, 1 wt% graphite, and 94 wt% MNPs fluid, following the same subsequent steps. These mixtures were then filled into a cylindrical mold, that had the same dimensions as the recess in the outer mold. The outer and inner molds with the respective mixture were then placed in a freezer at -18 °C for 12 hours, which froze the mixtures. Afterwards, they thawed at room temperature for 12 hours. Subsequently, the inner part was placed in the recess of the outer phantom. This freeze-thaw process was repeated once, for a total of two freeze-thaw cycles.

2.2 Magnetic Nanoparticles

The dextran-coated superparamagnetic iron oxide nanoparticles (Dex-SPIONs) employed in this study were produced and characterized by the Section of Experimental Oncology and Nanomedicine (SEON) at the University Hospital Erlangen [17]. These nanoparticles are versatile, finding applications as contrast agents in magnetic resonance imaging as well as in MDT. They exhibit an average hydrodynamic size of 20 nm. Their stock solution contains an iron content of 12 (mg Fe)/mL, which was diluted to 5 (mg Fe)/mL for the experiments.

2.3 Ultrasound Strain Elastography

USE maps the stiffness or elasticity of the imaged region of interest. Usually, USE images are generated by using an ultrasound transducer to measure biological tissue. Here, two sets of radiofrequency (RF) ultrasound datasets

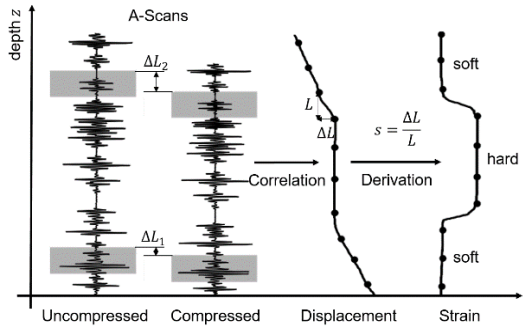

Fig. 3: Computing the strain rate with uncompressed and compressed radiofrequency data.

are captured under two different levels of mechanical compression. This mechanical compression can be either induced by pressing down the ultrasound transducer or through naturally occurring internal movements, such as vascular flow or breathing. In the case of phantom studies, no naturally occurring movements are induced, so mechanical compression using the ultrasound transducer was utilized.
The induced tissue displacement was then tracked between pairs of RF data before and after compression using 1D-correlation along the axial dimension, as illustrated in Fig. 3. For estimating the axial displacement u, two axial (in z segments of RF data are defined as:

$$r_1(n+k) = r_{RF}(x_i, z_{n+k}, t_1) \qquad (1)$$

and

$$r_2(n+k) = r_{RF}(x_i, z_{n+k}, t_2), \qquad (2)$$

where r_1 is an axial segment of an RF line before compression (t_1), and r_2 is a segment after compression (t_2). x_i represents the lateral position, while z_{n+k} denotes the central axial position, with $N/2$ neighbors above and below. k is the current axial pixel under consideration for displacement computation and n is a counter variable.
The normalized cross-correlation (NCC) between RF frames r_1 and r_2,

$$c_k(u) = \frac{\sum_{n=-N/2}^{N/2} R_1 \cdot R_2}{\sqrt{\sum_{n=-N/2}^{N/2} R_1^2 \cdot \sum_{n=-N/2}^{N/2} R_2^2}} \qquad (3)$$

is scaled by their respective standard deviation [18]. In equation (3), the formulation $R_1 = r_1(n+k)$ and $R_2 = r_2(n+k-u)$ are used. The necessary displacement for the maximum of the NCC function in equation (3) is the estimated displacement:

Tab. 1: Measurement scenarios used for magnetically enhanced ultrasound strain elastography. With two axial transducer positions (Trans 1 and Trans 2) and electromagnet powered on (Mag. On) or powered off (Mag. Off).

		Trans 1	Trans 2	Mag. On	Mag. Off
A.	r_1	■			■
	r_2		■		■
B.	r_1	■		■	
	r_2		■	■	
C.	r_1	■		■	
	r_2	■			■
D.	r_1	■		■	
	r_2		■		■

$$\hat{u}_k = \underset{u}{\operatorname{argmax}}\{c_k(u)\}. \quad (4)$$

Using this displacement, the relative strain rate

$$s_k = \frac{\hat{u}_k}{L} \quad (5)$$

can be computed, where L is the axial pixel size. USE allows only for the calculation of relative values, indicating that in resulting images, only variations in tissue stiffness, such as softer or harder regions, can be visualized (see Fig. 3). As a result, the strain values within each image are normalized to a range of 0 to 1 in this contribution. 0 indicates hard regions while 1 indicates soft regions.

In the case of magnetic nanoparticle imaging, other compression methods are viable. Alongside the compression induced by the ultrasound transducer, the magnetic force capable of displacing tissue perfused with MNPs can be utilized. This study examined the following mechanical influences and their combinations, as clearly in Tab. 1:

A. **Transducer compression**: For r_1, the magnet was turned off and transducer was in its default position. For r_2, the magnet was turned off and the transducer applies compression.
B. **Magnetically stiffening tissue in combination with transducer compression**: For r_1, the magnet was turned on and the transducer was in its default position. For r_2, the magnet was turned on and transducer applied compression.
C. **Magnetic compression**: For r_1, the magnet was turned on and the transducer was in its default position. For r_2, the magnet was turned off and the transducer was in its default position.
D. **Transducer and magnetic compression**: For r_1, the magnet was turned on and the transducer was in its default position. For r_2, the magnet was turned off and the transducer applied compression.

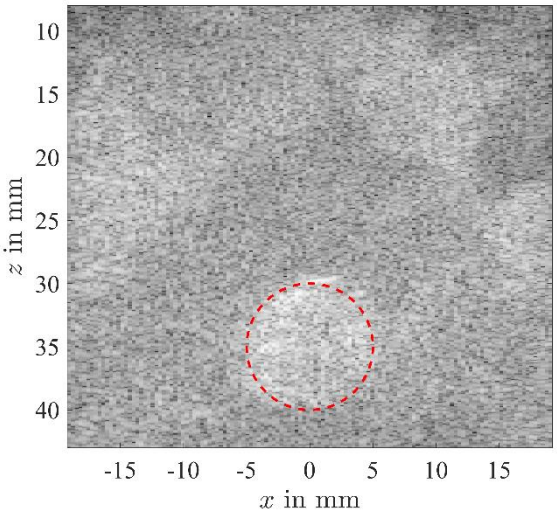

Fig. 4: Ultrasound B-mode image of a polyvinyl alcohol ultrasound phantom containing an inclusion of magnetic nanoparticles (marked as red dashed circle).

3. Results and Discussion

To assess the effectiveness of magnetically enhanced ultrasound strain elastography, ultrasound phantoms were constructed and subjected to sonographic measurements. Fig. 4 displays an ultrasound B-mode image of a phantom containing an inclusion of MNPs, indicated by a dashed red circle. Notably, the nanoparticle inclusion is not directly visible in the B-mode image without prior knowledge of its position.

For the elastographic assessments, a control phantom was fabricated to identify any potential errors in construction that might result in changes in stiffness. It was observed that even minor discrepancies in weighing the ingredients could significantly impact the resulting inclusion. Therefore, attention is required during the construction of such phantoms.

Among the repeated measurements of various control phantoms, no discernible changes in the resulting elastogram at 500 µm (1 % strain) were visible. At lower compression levels of 100 µm (0.2 % strain) areas of increased stiffness in the region of the inclusion occurred (although not in the same order as with MNPs). Fig. 5 demonstrates elastographic imaging of a control phantom at 0.2 % and 1 % strain. These

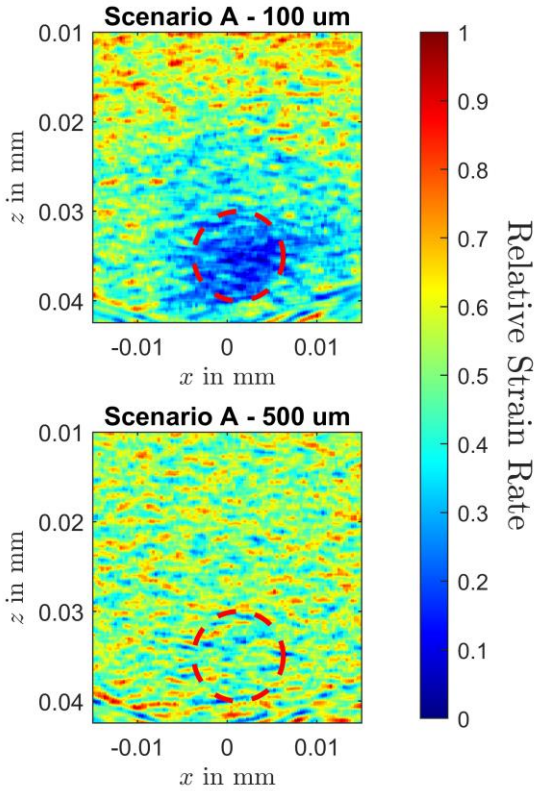

Fig. 5: Elastogram of control ultrasound phantom undergoing the same fabrication steps as the phantoms with magnetic nanoparticles, but with the same materials inside and outside.

results underscore the importance of precision in phantom construction and the difficulties of ultrasound strain imaging evaluation with MNPs.

In Fig. 6, the results from all measurement scenarios for PVA ultrasound phantoms with MNP inclusions are presented, with a transducer compression of 500 µm, corresponding to 1 % strain. In scenarios A, B, and D, similar elastographic images are depicted, while scenario C yields the clearest results. Scenario B and D have a slightly higher background contrast compared to Scenario A. Scenario C bears resemblance to magnetomotive ultrasound, wherein only the displacement of MNPs and surrounding tissue is induced, establishing a direct correlation with the MNP inclusion.

Scenarios C and D prove useful when limited compression is feasible, as magnetic displacement alone suffices for imaging purposes. Conversely, in a body with larger natural movements due to factors such as breathing, higher compression levels would naturally occur. Fig. 7 illustrates the results for higher compression level at 1000 µm (2 % strain) for scenario A and B. The elastogram using scenario A depicts no distinguishable difference between inclusion and surrounding phantom material. Scenario B

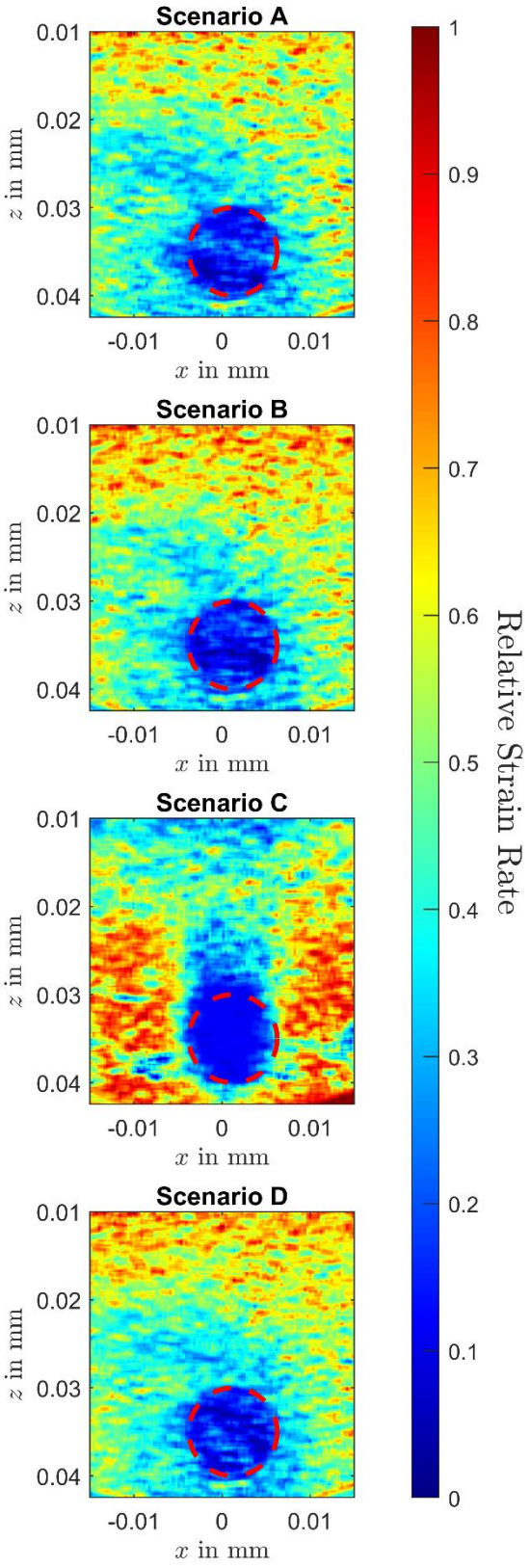

Fig. 6: Elastographic images of all measurement scenarios for a polyvinyl alcohol ultrasound phantom with an inclusion of magnetic nanoparticle and a transducer compression of 500 µm (1 % strain).

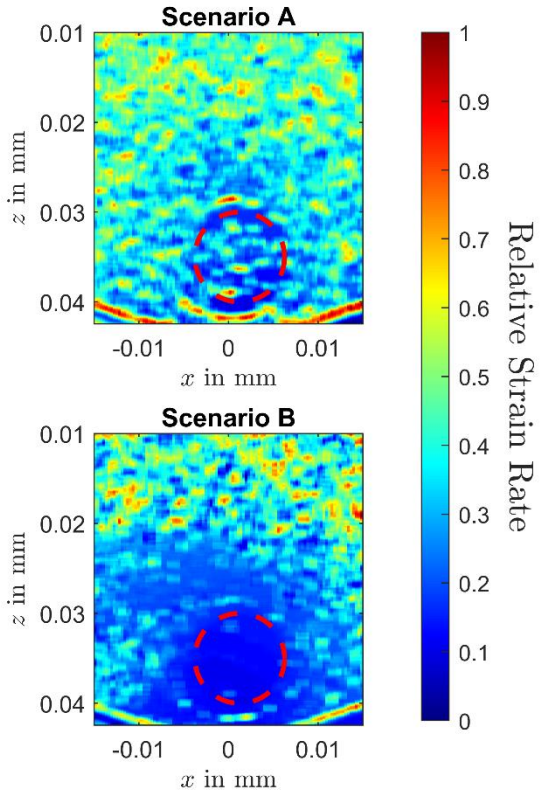

Fig. 7: Elastographic images of polyvinyl alcohol phantom with magnetic nanoparticle inclusion for scenario A and B with high compression of 1000 um (2% strain).

still demonstrates increased stiffness in the inclusion area, whereas not as clearly as with 1 % strain. MUSE possesses the ability to map larger areas of compression, as standard USE. This enhanced robustness for higher compressions is attributed to the magnetically induced increase in stiffness within the tissue perfused with MNPs.
These findings suggest that conventional USE can indeed visualize MNP distributions, but with the assistance of an MDT electromagnet, the imaging capabilities can be enhanced.

4. Conclusion

This study introduced a novel approach for mapping MNP distributions using a combination of USE and the magnetic force generated by an electromagnet used in MDT. This technique, termed “Magnetically Enhanced Ultrasound Strain Elastography” (MUSE), aims to augment the imaging capabilities of standard USE specifically for MNPs. The efficacy of MUSE was evaluated using two different ultrasound PVA phantoms, with measurements repeated three times using newly constructed phantoms.
One phantom served as a control, revealing areas of increased stiffness, but only at low compression levels. In contrast, the ultrasound phantoms containing MNP inclusions exhibited heightened stiffness. Under typical compression levels of 1 %, MUSE exhibits slightly improved imaging quality compared to conventional USE. At greater compression levels, the presence of the MNP inclusion remained detectable with MUSE, while USE failed. This suggests potential utility in scenarios involving naturally occurring movements.
Moreover, a technique similar to magnetomotive ultrasound could be employed at lower or negligible compression levels to establish a direct correlation with MNP distributions.
Future investigations should aim to explore the application of this method across varied elastic environments to better understand its limitations. Adjustments to the measurement setup are necessary, aligning the electromagnet on the same side as the ultrasound transducer to reflect practical scenarios. Moreover, animal studies should be conducted to further validate the efficacy and potential clinical utility of MUSE.

Acknowledgments

The authors gratefully acknowledge the financial support of the Deutsche Forschungsgemeinschaft (DFG) - project number 452821018.

References

[1] Sung, H., Ferlay, J., Siegel, R. L., Laversanne, M., Soerjomataram, I., Jemal, A., & Bray, F. (2021). Global cancer statistics 2020: GLOBOCAN estimates of incidence and mortality worldwide for 36 cancers in 185 countries. CA: a cancer journal for clinicians, 71(3), 209-249; doi: 10.3322/caac.21660.
[2] Lübbe, A. S., Alexiou, C., & Bergemann, C. (2001). Clinical applications of magnetic drug targeting. Journal of Surgical Research, 95(2), 200-206; doi: 10.1006/jsre.2000.6030.
[3] Tietze, R., Lyer, S., Dürr, S., Struffert, T., Engelhorn, T., Schwarz, M., Eckert, E., Göen, T., Vasylyev, S., Peukert, W., Wiekhorst, F., Trahms, L., Dörfler, A., & Alexiou, C. (2013). Efficient drug-delivery using magnetic nanoparticles—biodistribution and therapeutic effects in tumour bearing rabbits. Nanomedicine: Nanotechnology, Biology and Medicine, 9(7), 961-971; doi: 10.1016/j.nano.2013.05.001.
[4] George, B., Fink, M., Ermert, H., Rupitsch, S. J., Lyer, S., & Alexiou, C. (2019). Guiding and accumulation of magnetic nanoparticles employing high intensity focused ultrasound for drug targeting applications. Current Directions in Biomedical Engineering, 5(1), 589-592; doi: 10.1515/cdbme-2019-0148.
[5] Thalmayer, A. S., Götz, K., & Fischer, G. (2024). How the Magnetization Angle of a Linear Halbach Array Influences Particle Steering in Magnetic Drug Targeting—A Systematic

Evaluation and Optimization. Symmetry, 16(2), 148; doi: 10.3390/sym16020148.
[6] Paris, J. L., Mannaris, C., Cabañas, M. V., Carlisle, R., Manzano, M., Vallet-Regí, M., & Coussios, C. C. (2018). Ultrasound-mediated cavitation-enhanced extravasation of mesoporous silica nanoparticles for controlled-release drug delivery. Chemical Engineering Journal, 340, 2-8; doi: 10.1016/j.cej.2017.12.051.
[7] Huber, C., George, B., Rupitsch, S. J., Ermert, H., Ullmann, I., Vossiek, M., & Lyer, S. (2022, September). Ultrasound-Mediated Cavitation of Magnetic Nanoparticles for Drug Delivery Applications. In Current Directions in Biomedical Engineering (Vol. 8, No. 2, pp. 568-571). De Gruyter; doi: 10.1515/cdbme-2022-1145
[8] Avasthi, A., Caro, C., Pozo-Torres, E., Leal, M. P., & García-Martín, M. L. (2020). Magnetic nanoparticles as MRI contrast agents. Surface-modified Nanobiomaterials for Electrochemical and Biomedicine Applications, 49-91; doi: 10.1007/978-3-030-55502-3_3
[9] Borgert, J., Schmidt, J. D., Schmale, I., Rahmer, J., Bontus, C., Gleich, B., ... & Barkhausen, J. (2012). Fundamentals and applications of magnetic particle imaging. Journal of cardiovascular computed tomography, 6(3), 149-153; doi: 10.1016/j.jcct.2012.04.007
[10] Oh, J., Feldman, M. D., Kim, J., Condit, C., Emelianov, S., & Milner, T. E. (2006). Detection of magnetic nanoparticles in tissue using magneto-motive ultrasound. Nanotechnology, 17(16), 4183; doi: 10.1088/0957-4484/17/16/031
[11] Fink, M., Rupitsch, S. J., Lyer, S., & Ermert, H. (2021). Quantitative determination of local density of iron oxide nanoparticles used for drug targeting employing inverse magnetomotive ultrasound. IEEE Transactions on Ultrasonics, Ferroelectrics, and Frequency Control, 68(7), 2482-2495; doi: 10.1109/TUFFC.2021.3068791
[12] Uliana, J. H., Sampaio, D. R. T., Carneiro, A. A. O., & Pavan, T. Z. (2018). Photoacoustic-based thermal image formation and optimization using an evolutionary genetic algorithm. Research on Biomedical Engineering, 34, 147-156; doi: 10.1590/2446-4740.00218
[13] Huber, CM., El Aawar, K., Ermert, H., Ullmann, I., & Lyer, S. (2023, May). Visualization of Magnetic Nanoparticles by Ultrasound Strain Imaging. In Proceedings of the SMSI 2023 Conference – Sensor and Measurement Science International, pp. 344-345; doi: 10.5162/SMSI2023/P33
[14] Ophir, J., Cespedes, I., Ponnekanti, H., Yazdi, Y., & Li, X. (1991). Elastography: a quantitative method for imaging the elasticity of biological tissues. Ultrasonic imaging, 13(2), 111-134; doi: 10.1177/016173469101300201
[15] Alexiou, C., Diehl, D., Henninger, P., Iro, H., Rockelein, R., Schmidt, W., & Weber, H. (2006). A high field gradient magnet for magnetic drug targeting. IEEE Transactions on applied superconductivity, 16(2), 1527-1530; doi: 10.1109/TASC.2005.864457
[16] Fromageau, J., Gennisson, J. L., Schmitt, C., Maurice, R. L., Mongrain, R., & Cloutier, G. (2007). Estimation of polyvinyl alcohol cryogel mechanical properties with four ultrasound elastography methods and comparison with gold standard testings. IEEE transactions on ultrasonics, ferroelectrics, and frequency control, 54(3), 498-509; doi: 10.1109/TUFFC.2007.273.
[17] Unterweger, H., Tietze, R., Janko, C., Zaloga, J., Lyer, S., Dürr, S., Taccardi, N., Goudrouri, QM., Hoppe, A., Eberbeck, D., Schuber, DW., Boccaccini, AR., & Alexiou, C. (2014). Development and characterization of magnetic iron oxide nanoparticles with a cisplatin-bearing polymer coating for targeted drug delivery. International journal of nanomedicine, 3659-3676; doi: 10.2147/IJN.S63433
[18] Foster, S. G., Embree, P. M., & O'Brien, W. D. (1990). Flow velocity profile via time-domain correlation: Error analysis and computer simulation. IEEE transactions on ultrasonics, ferroelectrics, and frequency control, 37(3), 164-175; doi: 10.1109/58.55306